International Journal of Heat and Mass Transfer 52 (2009) 5878–5888

Contents lists available at ScienceDirect

International Journal of Heat and Mass Transfer

journal homepage: www.elsevier.com/locate/ijhmt

Characterization of a porous medium employing numerical tools: Permeability and pressure-drop from Darcy to turbulence

Federico E. Teruel [a,b,*], Rizwan-uddin [b,c]

[a] Centro Atómico Bariloche, CNEA, Bariloche 8400, Rio Negro, Argentina
[b] Department of Nuclear, Plasma and Radiological Engineering, University of Illinois at Urbana-Champaign, Urbana, IL 61801, USA
[c] National Center of Super Computing Applications, University of Illinois at Urbana-Champaign, USA

ARTICLE INFO

Article history:
Received 12 June 2009
Received in revised form 31 July 2009
Accepted 31 July 2009
Available online 9 September 2009

Keywords:
Porous media
REV
Permeability
Darcy–Forchheimer

ABSTRACT

A large set of microscopic flow simulations in the Representative Elementary Volume (REV) of a porous medium formed by staggered square cylinders is presented. For each Reynolds number selected, 10 different porosities are simulated in the 5–95% range. The Reynolds number is varied from $Re = 10^{-3}$ to $Re = 10^5$, covering the Stokes flow regime, the laminar flow regime and the turbulence flow regime. Low and moderate Reynolds number flow solutions ($Re \leqslant 200$) are achieved by numerically solving the 2D Navier–Stokes equations. Reynolds Averaged Navier–Stokes equations are employed to simulate the turbulence regime. Numerical results allow the investigation of the microscopic features of the flow as a function of the porosity and Reynolds number. Based on these microscopic results, the permeability of the porous medium is computed and a porosity-dependent correlation is developed for this macroscopic parameter. The Darcy–Forchheimer term or, equivalently, the friction factor, is also computed to characterize the porous medium for the complete range of porosity and Reynolds number simulated. The Forchheimer coefficient is found to be weakly dependent on the Reynolds number and strongly dependent on the porosity if the flow is fully turbulent. A porosity-dependent correlation is proposed for this quantity for high Reynolds numbers.

1. Introduction

The analysis of fluid flowing through porous media is required in a large range of applications in such industries as chemical, mechanical, nuclear, geological, environmental, petroleum, etc. The flow conditions encountered are broad enough to cover a large range of Reynolds numbers (*Re*) and a large range of porosities [1]. For example, Stokes flows in porous media may be encountered in ground water flows while turbulent flows are found in application such as heat exchangers or nuclear reactors. Several macroscopic parameters are often needed to complete the porous media models that are employed to describe such applications. This has motivated the research in the development of relationships to describe macroscopic parameters, such as permeability and Darcy–Forchheimer term, for different kinds of porous media and flow regimes (i.e. *Re*) [2–5].

The concept of permeability was introduced in early studies carried out by Darcy [6] who was investigating the resistance of a fluid to flow through a solid matrix. Permeability, according to Kaviany [1], may be understood to be a measure of the flow conductance of the solid matrix. Darcy found that the mass flow rate and the pressure gradient are related by the viscosity (fluid parameter) and permeability (a property of the porous medium and presumably independent of the flow conditions). This relationship, or Darcy law, may be written as:

$$-\nabla\langle P\rangle^f = \frac{\rho v}{K} U_D, \tag{1}$$

where v is the fluid viscosity, ρ is the density, K is the permeability, U_D is the Darcy, or space-averaged, velocity and $\langle P\rangle^f$ is the fluid-averaged pressure.

It is well documented that the inertial effects become significant in flows through porous media for $Re > 1$ (based on pore velocity and average pore diameter) [7]. Boundary layers start to develop on solid boundaries in this flow regime, and the relationship between the pressure gradient and the velocity is not linear. Darcy law is no longer valid, or alternatively, the permeability becomes a function of *Re*. One of the objectives of this study is to calculate the so called "true" permeability [8] or the permeability calculated for Stokes flow when the conditions are such that the Darcy law holds. The relationship between the pressure gradient and velocity in the inertial regime will be described by means of the Darcy–Forchheimer approximation that depends on the "true" permeability. Alternatively, an "apparent" permeability can be

---

[*] Corresponding author. Address: Centro Atómico Bariloche, CNEA, Bariloche 8400, Rio Negro, Argentina.
E-mail address: teruel@cab.cnea.gov.ar (F.E. Teruel).

0017-9310/$ - see front matter © 2009 Elsevier Ltd. All rights reserved.
doi:10.1016/j.ijheatmasstransfer.2009.07.017

Nomenclature

d	square-edge length
d_h	hydraulic diameter
f_{D-d}	friction factor based on Darcy velocity and d
f_{D-K}	friction factor based on Darcy velocity and K
k	turbulent kinetic energy
k_K	Kozeny constant
p	pore length scale
u	microscopic streamwise velocity
F	Forchheimer coefficient
H	REV's dimension (REV volume = $2H \times H$)
K	permeability
P	pressure
Re	Reynolds number
$Re_{\sqrt{K}}$	Reynolds number based on the fluid-averaged velocity and permeability
U_D	V-normalized space-averaged streamwise velocity, Darcy velocity
U	cross-section averaged streamwise velocity
V	volume of the REV
V_f	fluid volume inside the REV
Greek symbols	
ΔP	pressure-drop across the REV
ΔP^*	non-dimensional pressure-drop across the REV
ε	turbulent dissipation rate
ϕ	porosity
ν	kinematic fluid viscosity
ν_T	eddy viscosity
ρ	fluid density
Additional notations	
$\langle \Psi \rangle_f$	V_f-normalized space average of Ψ

employed to account for inertial effects in flow through porous media [8].

At high enough Re, when inertial effects become significant, experimental results show that the pressure-drop normalized with the square of the velocity is fairly constant [9]. Therefore, the momentum equation to describe flows in porous media has been empirically modified to capture this effect. The Darcy–Forchheimer equation (see for instance [10]) models the viscous (Darcy) and inertial behavior of the flow describing the pressure gradient in one dimensional flow as:

$$-\nabla \langle P \rangle^f = \frac{\rho \nu U_D}{K} + \frac{\rho F U_D^2}{\sqrt{K}}, \tag{2}$$

where the first term on the rhs is the Darcy law and the second one is the Forchheimer correction. F is the Forchheimer coefficient which is in general assumed to be dependent on the geometry of the media only. Note that Eq. (2) is sometimes called *Ergun* equation when the Forchheimer coefficient is replaced by the Ergun coefficient C_E. Additionally, it is worth mentioning that the term $F/\sqrt{K}$ is sometimes called the Forchheimer tensor [11].

Unfortunately, the Darcy–Forchheimer expression to describe drag forces in the momentum equation in porous media suffers from the fact that no general expression is available to describe the Forchheimer coefficient as a function of parameters of the solid matrix. Additionally, there are contrary evidences in literature regarding this coefficient's dependence on Re. For instance, Martin et al. [3] carried out numerical studies of periodic arrays of cylinders in cross flow, proposing a power-law dependence of the Forchheimer coefficient on the Re and porosity. On the other hand, Papathanasio and Markicevic [4] carried out a numerical evaluation of the Ergun and Forchheimer equations for hexagonal and square arrays of cylinders in cross flow, and unlike Martin et al. [3], these researchers proposed for the Forchheimer coefficient a dependence only on the porosity.

Theoretical studies have validated the inclusion of the Forchheimer (quadratic) term. Such studies have also led to suggestion of more complex descriptions to model the drag forces in the momentum equation for porous media. For example, based on length scale constraints and a theoretical analysis, Whitaker [12] showed that the Forchheimer term for high Re depends on the square of the velocity. Hsu and Cheng [13] considered the drag force in spheres placed in dilute systems to conclude that in addition to the Darcy–Forchheimer approximation, a *transitional* term describing the behavior of the boundary layer—that is formed between the Stokes flow regime and the inertial regime, where the flow is expected to separate from the surface of the sphere—is needed. This additional term is shown to be dependent on the velocity with a 3/2 power law. Experimental results obtained by Hsu et al. [14] show that the inclusion of this term improves the prediction of the pressure-drop by 20–30% for moderate Re.

The aim of this study is to compute the pressure-drop in a 2D porous medium formed by staggered square rods for different flow regimens. This is achieved by numerically simulating the flow field in a Representative Elementary Volume (REV) of the porous medium. The simulations cover the full range of flow regimes, from Stokes flows to fully turbulent flows ($10^{-3} < Re < 10^5$) and a large spectrum of the porosity (5–95%). The permeability and the Darcy–Forchheimer term are then computed as a function of porosity and Re from the results of these simulations. Correlations for these parameters are developed to help to characterize porous media models. Moreover, the dependence of the pressure-drop on the porosity and Re, at high Re, is analyzed and discussed.

This study is organized as follows. The next section is devoted to the description of the numerical method and geometry employed to compute the flow field inside the REV. The description of the numerical simulations carried out in this study for the Stokes, laminar and turbulent regimes follows. Microscopic flow fields for each flow regime are briefly described and analyzed. Microscopic results are integrated (i.e. volume-averaged) over the REV to obtain the permeability and pressure-drop. These results are presented in two consecutive Sections. In the first one, the permeability is computed as a function of porosity, and a correlation is developed for this quantity. In the second one, a *regime-map* of the friction factor as a function of the Re that covers all the flows regimens and employs the porosity as a parameter is created. Moreover, for the fully turbulent regime, a correlation for the friction factor as a function of porosity is developed and its dependence on the Re is discussed.

2. REV of the porous medium

The porous medium under consideration is formed by a 2D arrangement of staggered square rods (Fig. 1). The macroscopic flow field is assumed horizontal and the REV is chosen to be the rectangle 1234 (Fig. 1). The size of the square rods is varied from 0 to H to allow variations in the porosity. Numerical solutions are computed in this REV for different Re and for different porosities. Furthermore, these solutions are space-averaged to compute the macroscopic parameters of the porous medium.

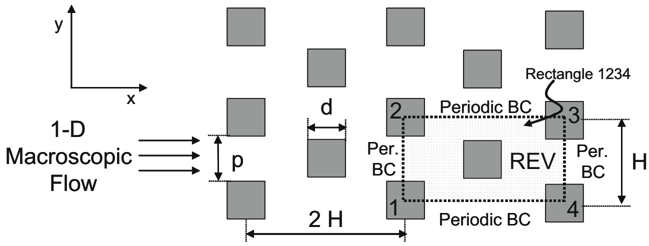

Fig. 1. REV of an infinite porous medium formed by staggered square rods.

2.1. Numerical method

Mass and momentum conservation equations are,

$$\frac{\partial u_i}{\partial x_i} = 0, \tag{3}$$

$$\frac{\partial u_i}{\partial t} + \frac{\partial}{\partial x_j} u_j u_i = -\frac{\partial p}{\partial x_i} + \frac{1}{Re}\frac{\partial}{\partial x_j}\frac{\partial u_i}{\partial x_j}. \tag{4}$$

For Stokes and laminar flow, the Navier–Stokes (N–S) equations (Eqs. (3) and (4)) are numerically solved in the REV for different *Re* and different porosities. For the turbulent regime, the Reynolds Averaged Navier–Stokes (RANS) equations are employed. In this case, the k–ε model with near wall treatment developed by Abe et al. [15] (*alias* AKN model) is used to model the Reynolds stresses. The momentum and transport equations for k and ε are (note that k and ε are made non-dimensional with U^2 and U^3/p, respectively),

$$\frac{\partial u_i}{\partial t} + \frac{\partial}{\partial x_j} u_j u_i = -\frac{\partial (p + 2k/3)}{\partial x_i} + \frac{\partial}{\partial x_j}\left[\left(\frac{1}{Re} + \nu_T\right)\left(\frac{\partial u_i}{\partial x_j} + \frac{\partial u_j}{\partial x_i}\right)\right], \tag{5}$$

$$\frac{\partial k}{\partial t} + \frac{\partial}{\partial x_j} u_j k = \nu_T\left(\frac{\partial u_i}{\partial x_j} + \frac{\partial u_j}{\partial x_i}\right)\frac{\partial u_i}{\partial x_j} + \frac{\partial}{\partial x_j}\left[\left(\frac{1}{Re} + \frac{\nu_T}{\sigma_k}\right)\frac{\partial k}{\partial x_j}\right] - \varepsilon, \tag{6}$$

$$\frac{\partial \varepsilon}{\partial t} + \frac{\partial}{\partial x_j} u_j \varepsilon = C_{\varepsilon 1}\nu_T \frac{\varepsilon}{k}\left(\frac{\partial u_i}{\partial x_j} + \frac{\partial u_j}{\partial x_i}\right)\frac{\partial u_i}{\partial x_j} + \frac{\partial}{\partial x_j}\left[\left(\frac{1}{Re} + \frac{\nu_T}{\sigma_\varepsilon}\right)\frac{\partial \varepsilon}{\partial x_j}\right] - C_{\varepsilon 2} f_\varepsilon \frac{\varepsilon^2}{k}. \tag{7}$$

The eddy viscosity and additional damping functions are computed as:

$$\nu_T = C_\mu f_\mu \frac{k^2}{\varepsilon}, \quad f_\mu = \left(1 - e^{\frac{-y^*}{14}}\right)^2 \left(1 + \frac{5}{R_t^{3/4}} e^{\frac{-R_t^2}{200}}\right),$$
$$f_\varepsilon = \left(1 - e^{\frac{-y^*}{3.1}}\right)^2 \left(1 - 0.3 e^{-\left(\frac{R_t}{6.5}\right)^2}\right), \tag{8}$$

where y is the distance to the closest wall and, $y^* = y\varepsilon^{1/4}Re^{3/4}$ and $R_t = k^2/\varepsilon Re$. Values of model constants are 0.09, 1.4, 1.4 1.5 and 1.9 for C_μ, σ_k, σ_ε, $C_{\varepsilon 1}$ and $C_{\varepsilon 2}$, respectively.

For all cases reported in this study, fully periodic boundary conditions are applied for the relevant variables over the boundaries of the REV (lines 1–2, 2–3, 3–4 and 4–1 in Fig. 1). Following boundary conditions are applied over the boundaries of the REV,

$$\begin{cases} \Psi(y)|_{1-2} = \Psi(y)|_{3-4} \\ \Psi(x)|_{2-3} = \Psi(x)|_{4-1} \end{cases} \text{and} \quad \begin{cases} P(y)|_{1-2} = P(y)|_{3-4} - \Delta P \\ P(x)|_{2-3} = P(x)|_{4-1} \end{cases}, \tag{9}$$

where Ψ is any velocity component or turbulence quantity, and ΔP is the driving force responsible for the motion of the fluid.

A standard N–S and RANS equation solver is implemented to compute the flow field in the REV. The solver is based on the finite control volume (FCV) technique, and the SIMPLER algorithm developed by Patankar [16]. Central difference and the QUICK scheme [17,18] are employed to, respectively, model the diffusion and the convective terms. The backward Euler scheme is used to advance in time. Additional details regarding solver implementation and validation are available in Ref. [19]. Only a brief description of the implementation of the periodic boundary conditions for the pressure field is specially addressed in this section due to its importance in the numerical solution.

The left/right boundary conditions of the REV (lines 1–2 and 3–4 in Fig. 1) are discussed first. Solutions of the N–S equations in periodic structures have been of great interest as many engineering applications require them (e.g. tube bundles, heat exchangers, porous media, etc.). Patankar et al. [20] for instance, described a method to implement the periodic boundary conditions in the context of the SIMPLE method. In the simulation of periodic structures, it is, in general, a standard practice to consider a driving force or pressure gradient that is responsible for the motion of the fluid resulting in a corresponding *Re* [20]. Alternatively, the mass flow rate may be prescribed and this driving force—that would lead to the prescribed mass flow rate—is then calculated [5,21]. In this study, a given fixed mass flow rate (or fixed *Re*) option is chosen, and hence the pressure-drop through the REV has to be calculated as part of the solution. This matter is resolved by considering a fixed pressure-drop (ΔP) in the x-direction as indicated in Eq. (9). An additional equation is therefore needed to calculate the pressure-drop ΔP (in comparison with the case of non-periodic flows). A constraint of constant mass flow rate provides this additional equation. The quantity ΔP must take a value so that the non-dimensional streamwise velocity averaged over the inlet section (or any vertical section) is equal to 1 (a normalized value). Mathematically, this can be expressed as:

$$\int_{\text{inlet}} u \, dy = 1. \tag{10}$$

Eq. (10) is solved for ΔP together with the x-momentum equation assuring that the mass flow rate is fixed at each time step. [Note that the solution for time dependent flows may be different if either the mass flow rate or the driving force is kept constant.]

The top/bottom boundary conditions (lines 2–3 and 4–1 in Fig. 1) are discussed next. The implementation of periodic boundary conditions on the top and bottom faces of the REV is relatively simple since no net pressure gradient exists in the vertical direction. However, it is important to note that periodic and symmetric boundary conditions are found in literature to model cases similar to the one being studied here (see for instance [22] for symmetric BCs or [23] for periodic ones). Both boundary conditions have been imposed in present simulations and, in general, they yielded the same solutions. Nevertheless, the solutions may differ if the problem turns out to be a time dependent one. The assumption of symmetry does not allow flow structures to move in the vertical direction from one cell to another while periodicity does. Additional comments will be made in this regard in Section 2.2.

The solver employed in this study has been fully tested and validated for a variety of geometries, including those presented in this study, as well as for a broad range of Reynolds numbers (see [19] for details). For example, the backward facing step (BFS) benchmark problem has been solved for validation purposes. In the laminar regime ($Re = 8 \times 10^2$), the results obtained by Gartling [24] have been reproduced with excellent agreement. In the turbulent regime, DNS results of Le et al. [25] ($Re = 5.1 \times 10^3$) and experimental results of Kim et al. [26] ($Re = 4.47 \times 10^4$) have been well captured.

2.2. Numerical simulations and microscopic results

The porous medium shown in Fig. 1 is again considered. The edge size of each square cylinder is d and the distance between cylinder's centers is H. The distance p (= $H - d$) is used as a measure of the pore size. Distance between square cylinders in the vertical direction, H, is fixed. Variables are normalized with the cell length

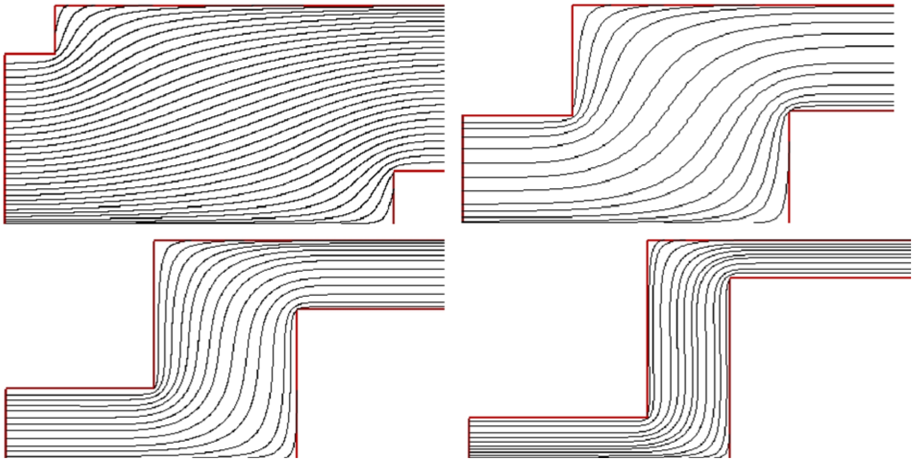

Fig. 2. Streamlines in one-quarter of the REV for $Re = 10^{-3}$. Porosities are 95%, 75%, 55% and 35% for panels from left to right and top to bottom, respectively.

scale (H) and the volume-averaged velocity, U_D (Darcy fluid velocity, $U_D = Up/H$, where U is the average inlet streamwise velocity over the cross-section p). The Reynolds number and porosity are, respectively,

$$Re = \frac{U_D H}{\nu}, \quad \phi = 1 - \left(\frac{d}{H}\right)^2. \tag{11}$$

Note that a constant Re implies constant mass flow rate.

Numerical simulations of the porous media cell (REV) shown in Fig. 1 are carried out for 10 different porosities, ranging from 5% to 95% and 10% interval, and different flow regimens that cover Stokes, laminar and turbulent flows. The initial conditions in all cases presented in this study are set in the entire domain as a constant streamwise velocity ($u = 1$) and zero vertical velocity. Uniform grids are employed for low Re flows while non-uniform grids are used for high Re laminar and turbulent flows (see Appendices A and B). Specific description for each flow regime follows.

2.2.1. Stokes flow

The first step to calculate the permeability as a function of porosity is to estimate the minimum grid resolution needed for the pressure-drop calculation (for given Re). Additionally, since a N–S equations solver is employed in this study to simulate Stokes flows, the magnitude of the Re that satisfactorily approximates the Stokes flow regime (K independent of Re) needs to be determined. In this regards, it can be pointed out that the permeability, given by Eq. (1), can be written as a function of Re and pressure-drop through the REV, as,

$$K = \frac{2}{\Delta P^{*} Re}\left(1 - \sqrt{1-\phi}\right)^2 H^2, \tag{12}$$

where $\Delta P^{*} (= \Delta P/\rho U^2)$ is the non-dimensional pressure-drop through the REV. Inspection of Eq. (12) shows that when the product of the pressure-drop through the cell and the Re is independent of this parameter [3], the flow is in the Stokes regime. Grid resolution of 10^4 control volumes per REV and $Re = 10^{-3}$ is determined to be sufficient for permeability calculations (see Appendix A).

Fig. 2 shows the streamlines of the flow for four different porosities and $Re = 10^{-3}$. No eddies are found for this range of Re at any porosity level [27]. The flow is symmetric about the horizontal line that divides the REV in two halves, and therefore only half of the REV may be simulated to obtain the same results as those presented here. Note that streamlines start and finish at the inlet and outlet sections of the domain, respectively.

2.2.2. Laminar flow

Based on REV simulations performed for low Re (permeability calculations) it was found that deviations from Darcy law are weak at $Re \approx 10$. Additionally, it is known [7] that oscillatory flow is found in porous media preceding the transition to turbulence for $Re \approx 150$. Therefore, a $Re = 10^2$ is selected to study laminar steady flows (where inertia is expected to play an important role in the flow features) and a set of numerical simulations is carried out. Pressure-drops in the REV are calculated as a function of porosity. The grid independence studies for laminar flow conditions that validate the former results are presented in Appendix B. [It is relevant to mention that direct simulations of the 2D N–S equations for Re above 150/200 resulted in oscillatory flow behavior. Three porosity cases—55%, 75% and 95%—were simulated to test this behavior. Movies showing the time dependent vorticity can be found in [28]. Modeling of time dependent, oscillatory laminar flow in porous media [10] is not the focus of this study and consequently these results are not discussed in this work.]

Flow features for the 10 different porosity cases for $Re = 10^2$, simulated using a *fine* grid (see Appendix B), are presented in Fig. 3 where one quarter of the REV is shown. The flow was found to be symmetric about the top and bottom horizontal lines of each domain. Fig. 3 shows the variation of streamlines patterns with porosity (red and blue colors show positive and negative vorticity values, respectively).[1] Different from the pattern found for low Re cases (Fig. 2), streamlines show the existence of several recirculation regions for $Re = 10^2$. At low porosities (Fig. 3), a recirculation region develops right after the corner of the first square. The size of this eddy is bounded by the length of the inlet section. (Note that the width of the vertical channel formed between the two squares is the same as the height of the inlet cross-section p.) A second eddy is also present at low porosities at the top symmetry line and over the vertical wall of the first square (clearly visible for porosities higher than 15% in Fig. 3). These two eddies merge at 35% porosity and the length of the resulting eddy over the vertical wall is then dictated by the size of the square (d). Its length over the symmetry line increases with porosity. At high porosities it depends also on d as the flow around one particular square is less affected by the others (Fig. 3). An eddy develops over the horizontal wall of the second square for porosities equal or above 35% and disappears for porosities above 85%.

---

[1] For interpretation of the references to color in this figure, the reader is referred to the web version of this paper.

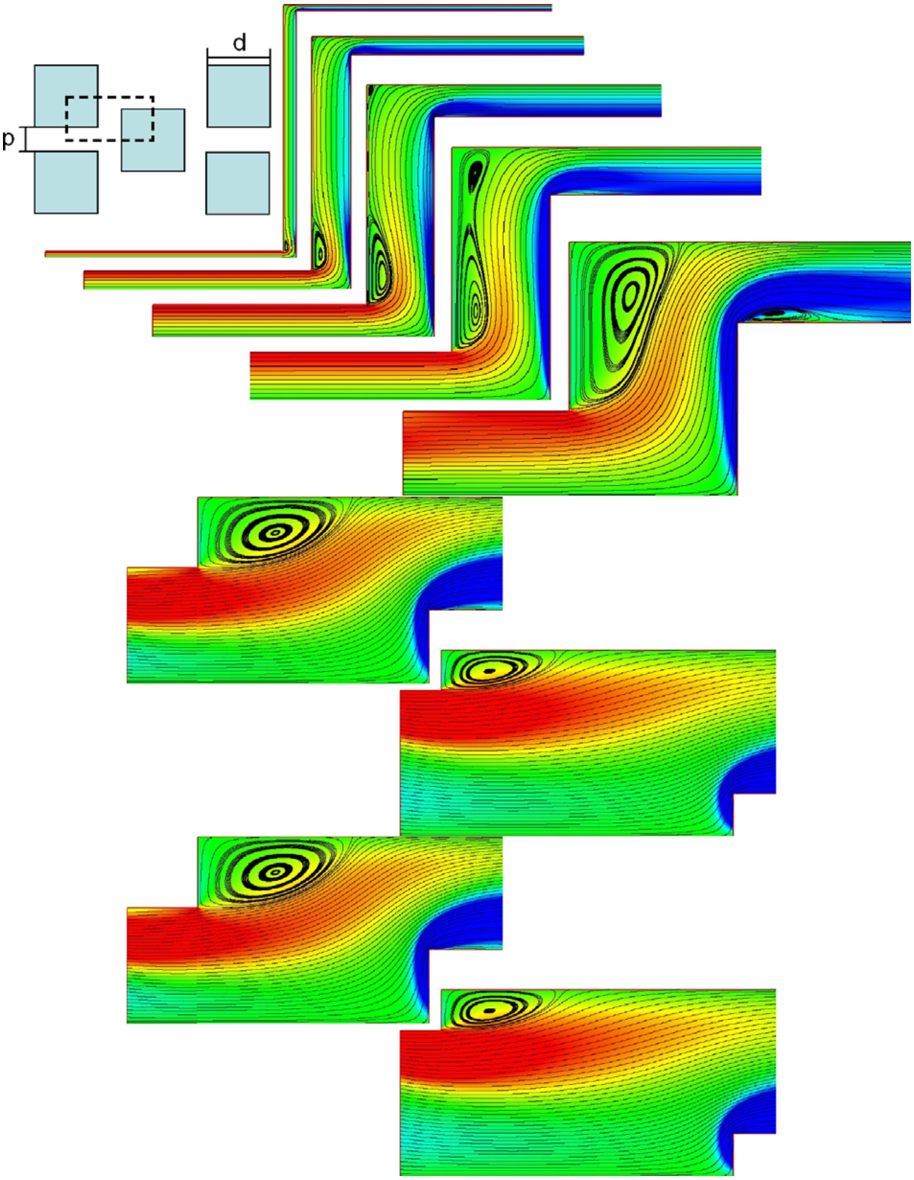

Fig. 3. Streamlines for 5–95% porosity in intervals of 10%. Porosity increases from top to bottom and from left to right; $Re = 10^2$.

2.2.3. Turbulent flow

Turbulent flow simulations are carried out employing the AKN k–ε model [15]. The simulated *Re* are 10^3, 3×10^3, 10^4 and 10^5. The *Re* range chosen to carry out the turbulent flow simulations starts with approximately the minimum *Re* at which the present implementation of the k–ε model does not break down and finishes with the fully turbulent regime at which the macroscopic pressure-drop are expected to be independent of this parameter [23].

A justification of the use of the AKN k–ε model is in order. Several authors [11,23,29,30] have reported extensive results of simulations in REVs of porous media for both, laminar and turbulent flows. These researchers employed k–ε models for turbulent flows obtaining steady-state solutions. However, at least for periodic cylindrical tube bundles, it has been shown that while the k–ε model predicts steady solutions, solutions found with LES feature vortex shedding and hence are time dependent [31,32]. It has also been shown that the three dimensionality of the flow at high *Re* [31] affects the distribution and characteristics of vortex shedding, and the results differ from those found in 2D simulations. Although all these evidence suggest that a detailed DNS/LES of a 3D domain involving several REVs may be needed to obtain an accurate representation of the flow field, the computational cost, in general, is too high. On the other hand, solution using the RANS equations permits simulation of a relatively large set of domains and *Re*. This has been of great help in understanding and developing further insight in the modeling of turbulence in porous media (e.g. see [23,33]). In particular, Kuwahara et al. [29] have recently reported a comparison of macroscopic quantities, for the same REV as that used in this work, obtained employing a 2D k–ε model and a 3D LES. A reasonable agreement was obtained and one of the claims of the study is that the k–ε models can be employed to estimate macroscopic quantities in the REV.

The porosity range as well as the range chosen for the *Re* in the present turbulent flow simulations are quite large and steady solutions are found in almost all cases. This may be attributable to the excessive dissipation of the k–ε model [32]. However, it should be noted that the results of numerical simulations reported by Kuwahara et al. (3D LES [29]), do not show vortex shedding. The only case in the present study that showed time dependence is for 95% porosity and $Re = 10^3$ [28]. This solution is periodic and clearly shows vortex shedding behind the solid squares.

One figure showing the turbulent flow field in the REV for different porosities and Re follow. Fig. 4 shows the streamlines for 55% porosity and four Re. Note that the size of the recirculation region behind the square increases slightly as Re is increased from $Re = 10^4$ to 10^5.

3. Computation of macroscopic parameters: permeability and Darcy–Forchheimer term

Microscopic results presented in Section 2.2 allow the computation of macroscopic parameters that are relevant to the macroscopic representation of the porous medium. The next two sections present the results obtained for the permeability and Darcy–Forchheimer term for the entire range of porosity and Re simulated.

3.1. Computation of permeability

Permeability and porosity (more precisely effective porosity) are both characteristics of the porous matrix. However, as pointed out by Kaviany [1, p. 27] no general relationship exists between these two parameters. Existing correlations are in general restricted to a constant porosity, range of porosities, type of matrix, etc. For example, the Carman–Kozeny equation is used in general to describe the permeability as a function of porosity [1]. Using the concept of hydraulic diameter and the Hagen–Poiseuille velocity in straight conduits, the permeability can be expressed as a function of the porosity, hydraulic diameter and the Kozeny constant (ϕ, d_h, k_K, respectively) as:

$$K = \frac{\phi d_h^2}{16 k_K}. \tag{13}$$

Microscopic solutions of the N–S equation in the REV shown in Fig. 1 can be used to determine the macroscopic pressure gradient and the Darcy velocity and therefore, the permeability by means of Eq. (12). It is noted that to relate the microscopic and macroscopic quantities in the REV, the gradient of the fluid-volume-averaged pressure that appears in the Darcy law (Eq. (1)) can be calculated as (see Fig. 1):

$$\begin{aligned}\nabla \langle P \rangle^f &= \nabla \left[\frac{1}{V_f} \int_{V_f} P\, dV \right] \\ &= \frac{1}{2H} \frac{1}{2H^2 \phi} \int_{V_f} [P(x+2H, y) - P(x, y)]\, dV = \frac{-\Delta P}{2H},\end{aligned} \tag{14}$$

where ΔP is again the pressure-drop across the cell. Note that periodicity in the pressure field has been used (Eq. (9)). Similarly, the Darcy velocity can be calculated as:

$$U_D = \frac{1}{V} \int_{V_f} u\, dV = \frac{1}{2H^2} \int_{2H} dx \int_H u\, dy = \frac{1}{2H^2} \int_{2H} Up\, dx = \frac{Up}{H}, \tag{15}$$

where U is the average inlet velocity and Up is the inlet flow rate in the REV. Using Eqs. (1), (14), and (15), Darcy law can be rewritten in the form of Eq. (12) as a function of the microscopic quantities where Re is based on the inlet flow rate (Up).

Microscopic results presented in Section 2.2 are used to calculate the permeability using Eq. (12). Results are shown in Fig. 5 where permeability is plotted as a function of the porosity with two different normalizations. Recalling the Carman–Kozeny approximation formula (Eq. (13)) and using the definition of the hydraulic diameter ($d_h = \phi/(1-\phi)d$ for the REV used here), the non-dimensional permeability may be written as:

$$\frac{K}{H^2} = \frac{1}{16 k_K} \frac{\phi^3}{(1-\phi)} \quad \text{or} \quad \frac{K}{d_h^2} = \frac{\phi}{16 k_K}. \tag{16}$$

The horizontal and vertical axes in Fig. 5 have been chosen based on these expressions. As expected, and shown in Fig. 5, for low porosities the permeability tends to zero, or equivalently, the pressure gradient tends to infinity for a fixed flow rate. Thus the numerical results agree very well with the Carmen–Kozeny equation for low porosity values. For large porosities, the numerically determined permeability does not follow the Carman–Kozeny equation. Recall that the Carmen–Kozeny relationship is based on treating the porous media as a network of capillaries, and hence it is not surprising that it does not hold for large values of porosities. The straight line in Fig. 5a—that shows the linear relationship

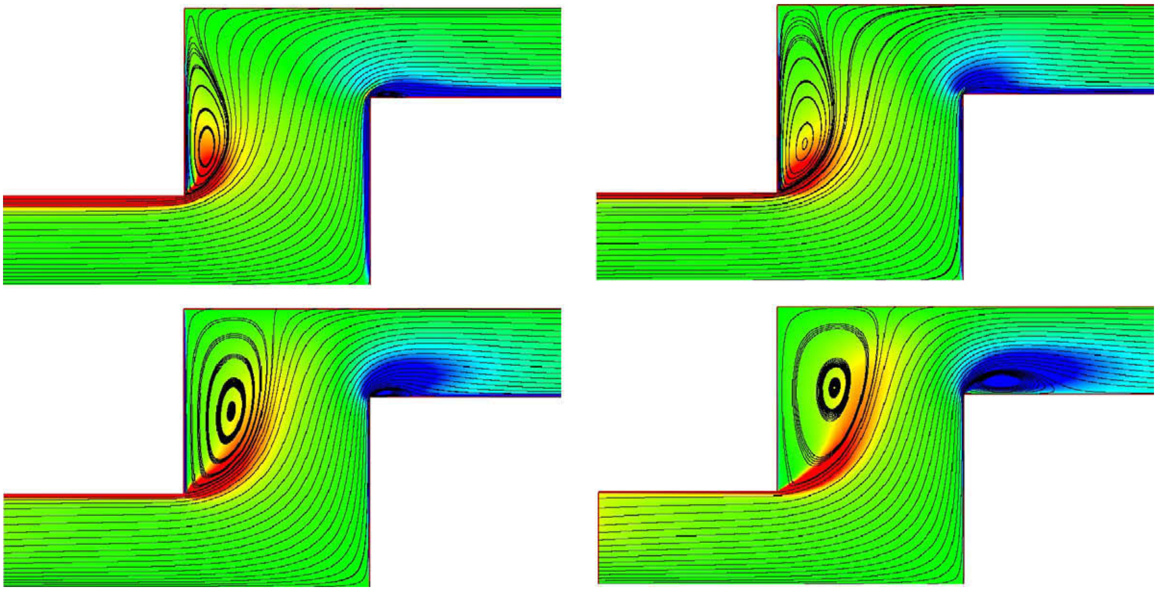

Fig. 4. Streamlines for 55% porosity. From left to right and top to bottom; $Re = 10^3$, 3×10^3, 10^4 and 10^5, respectively.

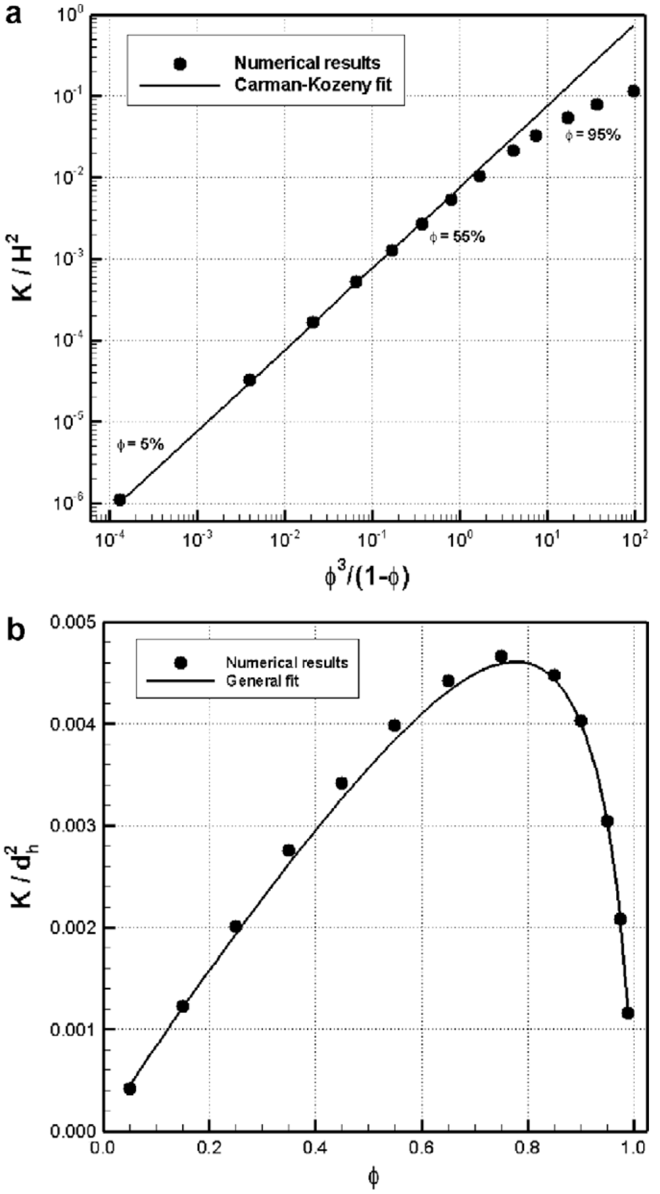

Fig. 5. Numerically calculated permeability as a function of porosity. (a) Permeability normalized with a fixed length dimension (H) and a linear fit *ala* Carmen–Kozeny. (b) Permeability normalized with a porosity dependent length dimension (d_h, hydraulic diameter) and a fitted curve given by Eq. (17). Note that the horizontal axes in the two panels are also different.

suggested by the Carmen–Kozeny equation—is obtained by fitting the numerical data over porosity values of (0, 0.45), or over (10^{-4}, 0.16) of the horizontal scale of the cartoon. The Kozeny constant that resulted from the fit is $16k_K = 131$. The fit based on the Carman–Kozeny theory matches the numerically calculated permeabilities within a 10% error for porosities lower than 55%. The disagreement between the numerically determined permeability values and those predicted by the Carmen–Kozeny equation (for high porosity values) is in agreement with the well known fact that the Kozeny constant is porosity dependent [1].

The numerically calculated values for the permeability are compared with similar results in literature obtained for the same geometry. Numerically calculated permeabilities were reported by Saada et al. [34] in the 10–90% porosity range. Reported values for 15%, 35%, 65% and 85% porosity are $K/H^2 \approx 3.0 \times 10^{-5}$, 5.0×10^{-4}, 5.3×10^{-3} and 2.2×10^{-2}, respectively. Corresponding values determined in this study are 3.3×10^{-5}, 5.2×10^{-4}, 5.3×10^{-3} and 2.2×10^{-2}. The agreement is fairly good over the entire porosity range.

Analytical studies of slow flow through periodic arrays of cylinders provide good insight regarding the dependence of permeability on porosity (see for instance Sangani and Acrivos [35]). In the limit of concentrated arrays ($\phi \to 0$), the approximations used in lubrication theory [36] can be employed to analytically solve the flow. It is found that the dependence of permeability on "solid concentration" (i.e. $1-\phi$) in this limit is a power law [35]. Additionally, in the limit of dilute arrays ($\phi \to 1$), the flow can be solved analytically [37]. The dependence of permeability in this limiting case involves logarithmic, linear and quadratic functions of the solid concentration [35]. Erdmann [38] studied in detail the permeability of different ordered porous media in transverse flows. He found that numerical fits based on the (theoretical) functional dependence on porosity in the limit of concentrated arrays are able to fairly represent the permeability over the entire range of porosity. A fit of this kind is shown in Fig. 5b, which functionally and parametrically is given by:

$$\frac{K}{H^2} = 0.306\left(1-(1-\phi)^{0.270}\right)^{2.910}. \qquad (17)$$

This fit captures the numerically calculated data points for permeability within 7% of accuracy over the entire porosity range considered.

3.2. Computation of pressure-drop: Darcy–Forchheimer term

As was pointed out in Section 1, the Darcy–Forchheimer equation models the viscous (Darcy) and inertial behavior of the flow describing the pressure gradient in one dimensional macroscopic flow (Eq. (2)). By analogy with the clear flow case, the pressure gradient in the porous media is often presented as a correlation between the *friction factor* and the *Re*. If Eq. (2) is made non-dimensional, the *friction factor* may be defined as:

$$f_{D-K} = -\frac{\nabla\langle P\rangle^f\sqrt{K}}{\rho U_D^2} = \frac{\nu}{\sqrt{K}U_D} + F = \frac{1}{Re_{D-K}} + F, \qquad (18)$$

where the pressure gradient is made non-dimensional with the square of the Darcy velocity and the square root of the permeability, and Re_{D-K} is the *Re* based on the Darcy velocity and the square root of the permeability. The aim of this section is to compute the friction factor in the transition from Stokes to laminar flow and, to turbulent flow, and to determine its dependence on porosity and *Re*.

Microscopic numerical results described in Section 2.2 are used to compute the friction factor defined in Eq. (18). For each pair of porosity and *Re*, the macroscopic pressure gradient through the porous cell is calculated using Eq. (14), and the Darcy velocity is calculated using Eq. (15). The numerically determined permeability (Fig. 5) is employed to calculate the *friction factor* and Re_{D-K}. The *friction factor* is calculated for the 10 porosities (5–95% with increments of 10%) and for the six different *Re* simulated (10^{-3}, 100, 10^3, 3×10^3, 10^4, 10^5), and is shown in Fig. 6a. Additionally, for porosities equal to 5%, 55% and 95%, results obtained for $Re = 10^{-2}$ and 10 are also included in Fig. 6a (see Appendix A).

Fig. 6a shows good agreement between the numerical data and Darcy law for all porosities up to $Re_{D-K} \approx 0.1$. Note that Darcy law begins to deviate from the experimental data for Re_{D-K} greater than 0.1 [1]. For $Re_{D-K} > 1$, results are also shown in Fig. 6b with a linear scale for the *friction factor*. Based on this figure, it may be concluded that the Forchheimer coefficient as well as the *friction factor* are fairly constant at fixed porosity. Hence, for this REV, the Forchheimer coefficient scales well with the square of the velocity and is assumed to be fairly independent of the *Re*. Moreover, as expected,

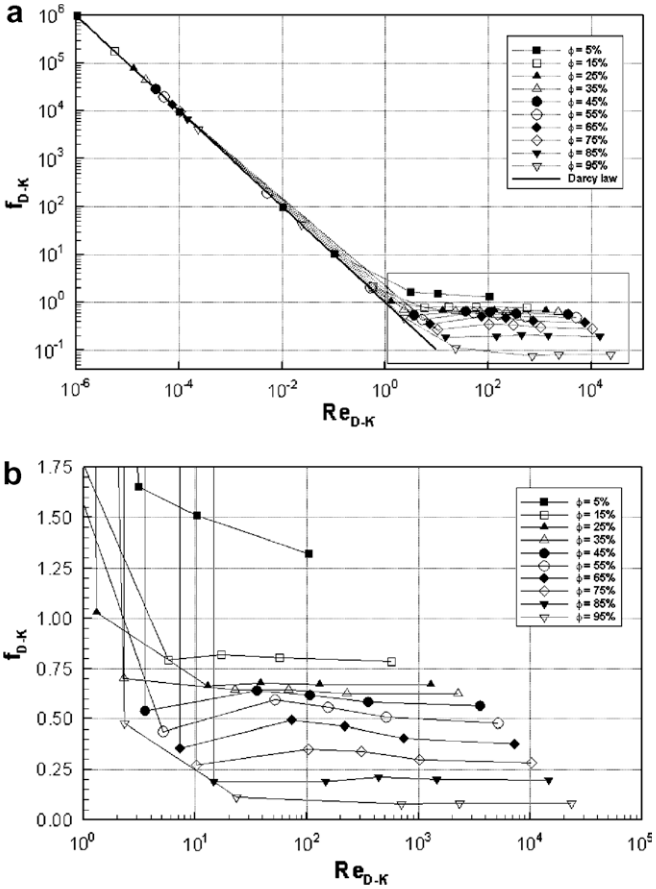

Fig. 6. *Friction factor* as a function of Re_{D-K} for 10 different porosities. (a) Complete *Re* range. (b) Inertial regime zoomed in.

a strong dependence on the geometry is found. Note that this coefficient is in general modeled to vary as a negative power of the porosity [10].

The analysis of the microscopic flow presented in Section 2.2 provides good insight to further understand results shown in Fig. 6b. As expected, the comparison of the microscopic flow for two different porosities shows that the size and location of eddies are strongly dependent on the porosity. For a constant porosity, however, slight variations of the microscopic flow were shown as the *Re* is increased from 10^4 to 10^5. This aspects are reflected in Fig. 6b which shows a strong dependence of the friction factor on the porosity and a fairly constant friction factor at high *Re* (turbulent regime).

In order to study the dependence of the Forchheimer coefficient on porosity in the fully turbulent regime and to compare present results with available published data, the pressure gradient is normalized as suggested by Kuwahara et al. [29]. For velocity this normalization employs the Darcy velocity. However, the edge size of the square rods (d) is used as the length scale. Noting that the contribution to the *friction factor* from the Darcy law is less than 1% for all porosities and for the highest Re_{D-K} number simulated, only the quadratic term is assumed to contribute to the *friction factor* in the following comparison. (See Fig. 6b for the ϕ = 5% case. The contribution from the Darcy law in this case is the largest, and $R_{D-K} = 10^2$ and $f_{D-K} = 1.25$. Hence, Darcy's contribution in less than 1%.) With this new normalization, the *friction factor* is written as:

$$f_{D-d} = -\frac{\nabla\langle P\rangle^f d}{\rho U_D^2} = \frac{Fd}{\sqrt{K}}. \tag{19}$$

Kuwahara et al. [29] presented numerical results for f_{D-d} evaluated at high *Re* for the same REV as that studied here. Those results are based on 3D simulations using LES and 2D simulations employing the k–ε model with near wall treatment. The porosity range in their study is 50–90%. Kuwahara et al. [29] found that the numerical results are reproduced fairly well in this range of porosity by the empirical Ergun's equation. This equation simply relates the friction factor and the porosity as:

$$f_{D-d} = 2.0\frac{1-\phi}{\phi^3}, \tag{20}$$

where the coefficient 2.0 was calculated by Kuwahara et al. [29] by fitting the numerical results (more commonly used value for this coefficient is 1.75 [1]). Fig. 7a shows results obtained by Kuwahara et al. [29] for high *Re*, present results for $Re = 10^5$ (based on *Up*) and 10 different porosities, and the Ergun's empirical equation fitted by Kuwahara et al. [29]. In the 50–90% porosity range, present results agree fairly well with those reported by Kuwahara et al. [29].

For porosities less than 40% (right side of Fig. 7a), present results depart from Ergun's equation. Additionally, it is noted in Fig. 7a that for low porosities the friction factor grows more slowly than at high porosities relative to the abscissa. Hence, for the 5–95% porosity range simulated in the present study a $(1-\phi)/\phi$ scale for the *friction factor* is found to be more appropriate. This is shown in Fig. 7b for $Re = 3\times10^3$, 10^4 and 10^5 along with a power-law fit with $(1-\phi)/\phi$,

$$f_{D-d} = 8.509\left(\frac{1-\phi}{\phi}\right)^{1.619}. \tag{21}$$

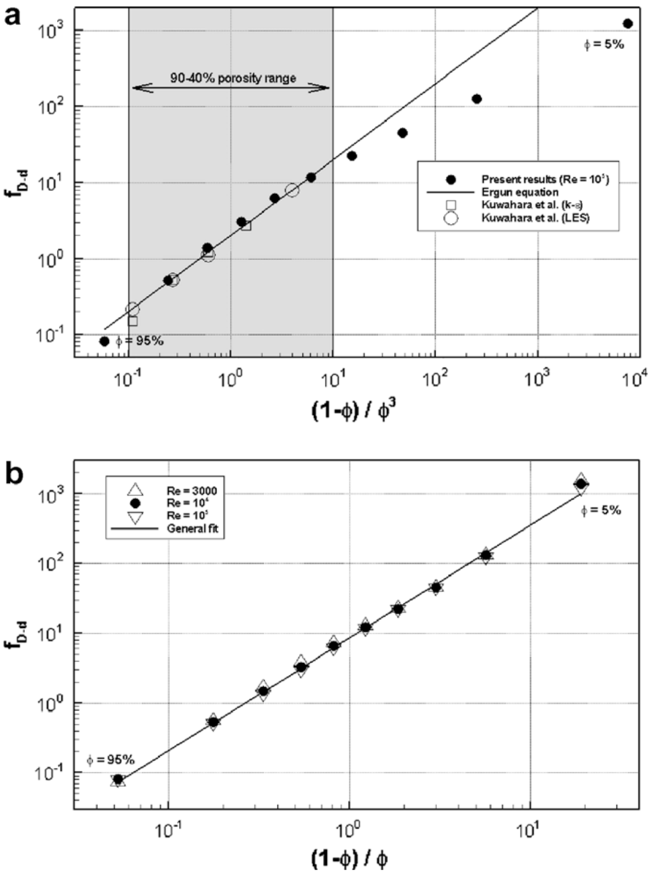

Fig. 7. *Friction factor* as a function of porosity for high *Re*. (a) Scaled with $(1-\phi)/\phi^3$. (b) Scaled with $(1-\phi)/\phi$ and fitted with Eq. (21).

This specific power-law fit leads to an error no greater than 5% in the 35–85% porosity range and an error that is less than 20% in the entire porosity range. [It is noted that by employing the correlations developed for the permeability, Eq. (17), and the one developed for the friction factor, Eq. (21), an analytical expression for the Forchheimer coefficient as a function of porosity can be found.]

4. Summary and conclusions

A large set of microscopic flow simulations of the REV of a porous medium formed by staggered square cylinders is presented in this study. These simulations are characterized by the imposition of periodic boundary conditions and are constrained to a constant mass flow rate. The flow distribution inside the REV is investigated for different flow regimes that cover eight orders of magnitude of the *Re* (from Stokes flows to turbulent flows). Symmetric and steady flows are encountered in the complete set of simulations with the exception of one case (with $Re = 10^3$ and 95% porosity) that results in a time dependent flow. For *Re* greater than 150–200 (laminar flow), direct numerical simulations of the N–S equations result in time dependent solutions (at least for the 55–95% porosity range).

Simulations of Stokes flows are carried out using a N–S equation solver. The flow is characterized by open streamlines that enter and leave the periodic computational domain. Based on the results of numerical simulations, it is found that the semi-analytical Carman–Kozeny equation commonly used to estimate permeability as a function of porosity does not capture the permeability's dependence on porosity over porosity range of $5\% < \phi < 95\%$. Therefore, a new correlation for the permeability of the medium as a function of porosity is developed by fitting to the numerically obtained data. This correlation captures the relationship over the entire range of porosity studied here (5–95%) better than the Carmen–Kozeny equation, and can be employed in macroscopic numerical models to compute the permeability as a function of porosity assuring errors below 7% in 5–95% porosity range.

Laminar flow simulations clearly show a dominant inertial component compared to the viscous-dominated Stokes flows. A core flow passing through the REV and several recirculation regions attached to the solid walls are identified in microscopic simulations. For $Re = 10^2$, a deviation from Darcy law is noted for porosities greater than 15%.

Microscopic solutions in the turbulence regime show, as in the laminar case, the formation of recirculation regions and a core flow passing through the REV. The microscopic solutions for high enough *Re* ($Re \geqslant 10^4$) are weakly dependant on this parameter. This translates to a fairly constant pressure-drop across the cell in this high *Re* regime.

The Darcy–Forchheimer approximation, or equivalently, the friction factor, is fully characterized for the porous medium analyzed in this study. The Forchheimer coefficient is found to be strongly dependent on the porosity and fairly independent of the *Re* in the turbulent regime. The Ergun equation is shown to be appropriate only for a limited range of porosities. If the entire range of porosity is considered, the friction factor (f_{D-d}) can be better approximated by a power law as a function of $(1-\phi)/\phi$. A correlation was developed for the friction factor at high *Re*. This correlation assures errors below 20% over the entire range of porosity studied in this work.

Appendix A. Grid independence study for low *Re* flow simulations

As the objective of the low *Re* flow simulations is to calculate the REV's permeability, this grid independence study is focused on the accuracy of the results obtained for the pressure-drop through the cell and the product of the pressure-drop and *Re*. Table A.1 shows the results for the non-dimensional pressure-drop for $Re = 10^{-3}$ and three different porosities (5%, 55% and 95%) as a function of the grid resolution. For each case presented in Table A.1, uniform grid resolutions are chosen so that approximately 5×10^3 (*Coarse*), 10^4 (*Fine*) and 2×10^4 (*Finest*) control volumes (CVs) resulted in successively refined discretizations. Employing Richardson's extrapolation [39] and based on results of the three grids considered, the pressure-drop is extrapolated. This value is presented in Table A.1 together with the order of accuracy obtained for the Richardson extrapolation. Moreover, the product of the pressure-drop and *Re* is also shown for different inlet flow rates corresponding to $Re = 10^{-1}$ and $Re = 10$ (for the *fine* grid case only).

Results reported in Table A.1 show that the error in the pressure-drop calculated with the *fine* grid ($\approx 10^4$ CVs) with respect to the extrapolated value is within 1% for the three porosities considered. Additionally, Table A.1 shows that the conditions for the *Re* of 10^{-3} correspond to Stokes flow. Note that the product of pressure-drop and the *Re* for $Re = 10^{-1}$ resulted in the same values as that for $Re = 10^{-3}$ case (at least within three significant figures). It is thus concluded that permeability values are accurately calculated using a grid resolution of 10^4 CVs per domain and a *Re* of 10^{-3} for all porosities considered in this study.

Appendix B. Grid independence study for moderate and high *Re* number flows

Realizing that the purpose of these simulations is to calculate the pressure-drop through the cell, the grid convergence is tested by tracking this macroscopic variable. Large variation in the REV's geometry over the range of porosity simulated in this study poses a challenge for the grid independence study since it is time consuming and impractical to carry out a separate study for each porosity and each *Re*. (The inlet section's *p*/*H* changes from 0.025 to 0.77 over the porosity range considered.) As the *Re* is based on the inlet flow section (*p*, Fig. 1) for both, laminar and turbulent flows, it is assumed that flow structures can be resolved with the same *p*-normalized CV size, independent of the porosity. Therefore, if a vertical discretization of the inlet section is determined to be sufficiently refined in a grid refinement study for a particular porosity, the same discretization is assumed to be sufficient for all other porosities when dimensions are normalized with *p*. Based on this assumption, it is convenient to carry out grid independence studies for the 75% porosity case. This porosity has the advantage of possessing only two horizontal lines that define solid walls. Hence, this porosity requires less grid points than other porosities for the same resolution.

The strategy selected to define the computational grid at different porosities and fixed *Re* yields an average mesh size (*p*-normalized) that increases when porosity is reduced. For low porosities, *p* is small relative to the REV size and hence the *p*-normalized domain becomes large. The use of non-regular grids that cluster points near the walls yields large cells in regions located far away from the corners of the solid squares. Hence, to employ the same discretization for the inlet section independent of the porosity yields an average mesh size (*p*-normalized) that increases when porosity is reduced. For this reason, grid independence studies are carried out for the lowest porosity under consideration (5%) in addition to the 75% porosity case. To avoid excessive computational time, less resolved meshes than in the 75% porosity case are employed in the 5% porosity case. Moreover, for the sake of completeness, the other end of the porosity spectrum studied here (95%) is also considered in the grid independence study and corresponding results can be found in [19]. Non-regular grids that

Table A.1
Grid independent study for 5%, 55% and 95% porosities. Last row for each porosity level shows the (Richardson) extrapolated value for the pressure-drop and the order of convergence. Results for the fine grid and $Re = 10^{-1}$ and 10 cases are also shown for each porosity.

Porosity	Grid–CVs per inlet section	ΔP^*	Re	$\Delta P^* Re$
$\phi = 0.05$ ($p/H = 0.025$)	6 (Coarse)	1.161 E+06	10^{-3}	1.161 E+03
	8 (Fine)	1.167 E+06	10^{-3}	1.167 E+03
	10 (Finest)	1.170 E+06	10^{-3}	1.170 E+03
	8	1.167 E+04	10^{-1}	1.167 E+03
	8	1.170 E+02	10	1.170 E+03
	Extrapolated value (order = 2.0)	1.175 E+06		
$\phi = 0.55$ ($p/H = 0.329$)	22 (Coarse)	8.109 E+04	10^{-3}	8.109 E+01
	30 (Fine)	8.093 E+04	10^{-3}	8.093 E+01
	44 (Finest)	8.079 E+04	10^{-3}	8.079 E+01
	30	8.093 E+02	10^{-1}	8.093 E+01
	30	8.441 E+00	10	8.441 E+01
	Extrapolated value (order = 0.7)	8.028 E+04		
$\phi = 0.95$ ($p/H = 0.776$)	10 (Coarse)	2.210 E+04	10^{-3}	2.210 E+01
	16 (Fine)	2.198 E+04	10^{-3}	2.198 E+01
	22 (Finest)	2.193 E+04	10^{-3}	2.193 E+01
	16	2.198 E+02	10^{-1}	2.198 E+01
	16	2.463 E+00	10	2.463 E+01
	Extrapolated value (order = 1.2)	2.183 E+04		

cluster points near walls are employed for the complete set of laminar and turbulent flow simulations. The formula that defines the grid point's locations can be found in Tannhehill et al. [40, p. 335] or Teruel [19].

A particular consideration in turbulent flow simulations is the distance of the first computational point to the wall. In general, for turbulence models with near wall treatment (e.g. AKN model employed here), it is recommended to locate this point at a distance lower than 1 (+units). Because the *friction velocity* is not known *a priori*, the strategy followed here is based on the calculation of $y^+ = 1$ for the fully developed turbulent channel flow with the same parameters (p, Re) as those that exist at the inlet section of the REV. Approximately, half of this value is then used to define the location of the point closest to the wall. In general, this strategy yields a posteriori y^+ values lower than 10 in the poorest resolved locations which are on the front-vertical walls of the squares (i.e. where the flow impinges). Grid sensitivity studies are carried out to evaluate the influence of the location of the first grid point from the wall.

For the sake of space, the grid independence study for the laminar case ($Re = 10^2$) is not presented here. Note that from the grid resolution point of view the turbulent case is more demanding than the laminar case. It is however pointed out that 48 CVs across the inlet section were employed. This grid yields errors within 1% with respect to the extrapolated values.

A grid independence study is carried out for $Re = 10^4$. Five different grids are considered for the 75% porosity case. The location of the first point normal to the wall is kept fixed. For this Re this location is 1×10^{-3} ($y^+ = 1$ corresponds to $y_1/p = 1.68 \times 10^{-3}$ in channel flow simulations). An additional grid is simulated where the location of the first point is five times closer to the wall than in previous grids ($y_1/p \approx 2 \times 10^{-4}$). Table B.1 shows the results for grids ranging from 24 to 96 CVs across the inlet section. The *fine* grid (48 CVs across the inlet section) has acceptable computational cost and leads to errors within 1% with respect to the extrapolated values. To evaluate the sensitivity of the results to the location of the first computational point from the wall, results for a grid with 68 CVs across the inlet section are also shown in Table B.1 ($y_1/p \approx 2 \times 10^{-4}$, y_1-reduced grid). The *fine* grid shows results within 1% of the y_1-reduced grid.

Considering more modest grid resolutions than in the 75% porosity case, a grid study is carried out for 5% porosity case. Table B.2 shows the 5% case where the more resolved grid corresponds to 48 CVs across the inlet section. Fine grid results are within an error of 1% of the extrapolated values. Moreover, the error with respect to the y_1-reduced grid is also within 1%. Note that the 5% porosity case is expected to yield the largest errors of all porosity cases as the p-normalized average mesh size is the largest. Based on this grid refinement study, it is concluded that a grid with 48 CVs across the inlet section and $y_1/p = 0.001$ is a good compromise between computational cost and accuracy for all porosities.

No grid independence study is carried out for Re equal to 10^3 and 3×10^3. A *fine* grid is employed for the calculation of all porosities with 48 CVs across the inlet section. A shorter version of the grid refinement study is conducted for 75% porosity and $Re = 10^5$. This study is similar to the one presented above for $Re = 10^4$ results

Table B.1
Grid independence study for 75% porosity and $Re = 10^4$. The average mesh size is calculated as the area of the domain divided by the number of grid points. The order of extrapolation as well as the extrapolated values is calculated using the fine, fine-2 and the finest grids.

CVs across the inlet section	Averaged mesh size (p-normalized)	ΔP^*
24 (Coarse)	0.0417	1.476
34 (Medium)	0.0294	1.464
48 (Fine)	0.0208	1.460
68 (Fine-2)	0.0147	1.458
96 (Finest)	0.0104	1.457
68 (y_1-reduced)	0.0147	1.466
Order of extrapolation		2.25
Extrapolated value		1.456
% Error fine grid to extrapolated value		0.2
% Error fine grid to y_1-reduced grid		0.4

Table B.2
Grid independence study for 5% porosity and $Re = 10^4$.

CVs across the inlet section	Average mesh size (p-normalized)	ΔP^*
24 (Coarse)	0.1383	1.898
34 (Medium)	0.0978	1.860
48 (Fine)	0.0687	1.845
48 (y_1-reduced)	0.0724	1.849
Order of extrapolation		2.88
Extrapolated value		1.837
% Error fine grid to extrapolated value		0.4
% Error fine grid to y_1-reduced grid		0.2

are given in Teruel [19]. It is shown that a grid with 60 CVs across the inlet section and with $y_1/p = 1.3 \times 10^{-4}$ is sufficiently refined to calculate the pressure-drop for all porosities (errors below 1%) for this *Re*.

References

[1] M. Kaviany, Principles of Heat Transfer in Porous Media, Springer-Verlag, 1991.
[2] S.L. Lee, J.H. Yang, Modeling of Darcy–Forchheimer drag for fluid flow across a bank of circular cylinders, Int. J. Heat Mass Transfer 40 (1997) 3149–3155.
[3] A.R. Martin, C. Saltiel, W. Shyy, Friction losses and convective heat transfer in sparse, periodic cylinder arrays in cross flow, Int. J. Heat Mass Transfer 41 (1998) 2383–2397.
[4] T.D. Papathanasiou, B. Markicevic, A computational evaluation of the Ergun and Forchheimer equations for fibrous porous media, Phys. Fluids 13 (2001) 2795–2804.
[5] D.G. Roychowdhury, S.K. Das, T. Sundararajan, Numerical simulation for laminar flow and heat transfer over banks of staggered cylinders, Int. J. Numer. Methods Fluids 39 (2002) 23–40.
[6] H. Darcy, Les Fontaines Publiques de la ville de Dijon, Dalmont, Paris, 1856.
[7] A. Dybbs, R.V. Edwards, A new look at porous media fluid mechanics – Darcy to turbulent, in: Fundamentals of Transport Phenomena in Porous Media, Martinus Nijhoff, 1984, pp. 199–256.
[8] D.A. Edwards, M. Shapiro, P. Bar-Yoseph, M. Shapira, The influence of Reynolds number upon the apparent permeability of spatially periodic arrays of cylinders, Phys. Fluids A 2 (1990) 45–55.
[9] I.F. Macdonald, M.S. El-Sayed, K. Mow, F.A.L. Dullien, Flow through porous media—the Ergun equation revisited, Ind. Eng. Chem. Fundam. 18 (1979) 199–208.
[10] C.T. Hsu, Dynamic modeling of convective heat transfer in porous media, in: Handbook of Porous Media, Taylor & Francis, 2005, pp. 39–80.
[11] A. Nakayama, F. Kuwahara, T. Hayashi, Numerical modelling for three-dimensional heat and fluid flow through a bank of cylinders in yaw, J. Fluid Mech. 428 (2004) 139–159.
[12] S. Whitaker, The Forchheimer equation: a theoretical development, Transp. Porous Media 25 (1996) 27–61.
[13] C.T. Hsu, P. Cheng, Thermal dispersion in porous media, Int. J. Heat Mass Transfer 33 (1990) 1587–1597.
[14] C.T. Hsu, H. Fu, P. Cheng, On pressure–velocity correlation of steady and oscillating flows in regenerators made of wire screens, J. Fluids Eng. 121 (1999) 52–56.
[15] K. Abe, T. Kondoh, Y. Nagano, A new turbulence model for predicting fluid flow and heat transfer in separating and reattaching flows-l flow field calculations, Int. J. Heat Mass Transfer 37 (1994) 139–151.
[16] S.V. Patankar, Numerical Heat Transfer and Fluid Flow, Hemisphere, 1980.
[17] B.P. Leonard, A stable and accurate convective modeling procedure based on quadratic upstream interpolation, Comput. Methods Appl. Mech. Eng. 19 (1979) 59–98.
[18] T. Hayase, J.A.C. Humphrey, R. Greif, A Consistently formulated QUICK scheme for fast and stable convergence using finite-volume iterative calculation procedures, J. Comput. Phys. 98 (1982) 108–118.
[19] F.E. Teruel, Macroscopic turbulence modeling and simulation for flow through porous media, Ph.D. Thesis, University of Illinois, Urbana-Champaign, IL, 2007.
[20] S.V. Patankar, C.H. Liu, E.M. Sparrow, Fully developed flow and heat transfer in ducts having streamwise-periodic variations of cross-sectional area, J. Heat Transfer 99 (1977) 180–186.
[21] G. Segal, K. Vuik, K. Kassels, On the implementation of symmetric and antisymmetric periodic boundary conditions for incompressible flow, Int. J. Numer. Methods Fluids 18 (1994) 1153–1165.
[22] M.H.J. Pedras, M.J.S. de Lemos, Computation of turbulent flow in porous media using a low-Reynolds k–ε model and an infinite array of transversally displaced elliptic rods, Numer. Heat Transfer Part A 43 (2003) 585–602.
[23] A. Nakayama, F. Kuwahara, A macroscopic turbulence model for flow in a porous medium, J. Fluids Eng. 121 (1999) 427–433.
[24] D.K. Gartling, A test problem for outflow boundary conditions—flow over a backward-facing step, Int. J. Numer. Methods Fluids 11 (1990) 953–967.
[25] H. Le, P. Moin, J. Kim, Direct numerical simulations of turbulent flow over a backward-facing step, J. Fluid Mech. 330 (1997) 349–374.
[26] J. Kim, S.J. Kline, J.P. Johnston, Investigation of a reattaching turbulent shear layer: flow over a backward-facing step, J. Fluids Eng. 102 (1980) 302–308.
[27] H.K. Moffatt, Viscous and resistive eddies near a sharp corner, J. Fluid Mech. 18 (1964) 1–18.
[28] Available from: <http://cabmec1.cnea.gov.ar/show/porousmedia/movies>.
[29] F. Kuwahara, T. Yamane, A. Nakayama, Large eddy simulation of turbulent flow in porous media, Int. Commun. Heat Mass Transfer 33 (2006) 411–418.
[30] M.J.S. de Lemos, Turbulence in Porous Media: Modeling and Applications, Elsevier, 2006.
[31] S. Benhamadouche, D. Laurence, LES, coarse LES, and transient RANS comparisons on the flow across a tube bundle, Int. J. Heat Fluid Flow 24 (2003) 470–479.
[32] D. Bouris, G. Bergeles, Two dimensional time dependent simulation of the subcritical flow in a staggered tube bundle using a subgrid scale model, Int. J. Heat Fluid Flow 20 (1999) 105–114.
[33] M.H.J. Pedras, M.J.S. de Lemos, Macroscopic turbulence modeling for incompressible flow through undeformable porous media, Int. J. Heat Mass Transfer 44 (2001) 1081–1093.
[34] M.A. Saada, S. Chikh, A. Campo, Analysis of hydrodynamics and thermal dispersion in porous media by means of a local approach, Heat Mass Transfer 42 (2006) 995–1006.
[35] A.S. Sangani, A. Acrivos, Slow flow fast periodic arrays of cylinders with application to heat transfer, Int. J. Multiphase Flow 3 (1982) 193–206.
[36] J. Happel, H. Brenner, Low Reynolds Number Hydrodynamics with Special Applications to Particulate Media, Prentice-Hall, Inc., NJ, 1965.
[37] D.L. Koch, J.C. Ladd, Moderate Reynolds number flows through periodic and random arrays of aligned cylinders, J. Fluid Mech. 349 (1997) 31–66.
[38] R.G. Erdmann, Image-based numerical simulation of Stokes flow in porous media, Ph.D. Thesis, University of Arizona, 2006.
[39] C.J. Freitas, U. Ghia, I. Celik, P. Roache, P. Raad, Asme's quest to quantify numerical uncertainty, AIAA Paper 2003-0627.
[40] J.C. Tannehill, D.A. Anderson, R.H. Pletcher, Computational Fluid Mechanics and Heat Transfer, second ed., Taylor and Francis, 1997.